2012

Thomson-resonant Interference Effects in Elastic X-ray Scattering Near the Cl K Edge of HCl

Stephane Carniato
University of Paris

P. Selles
University of Paris

Loic Journel
University of Paris

Renaud Guillemin
University of Paris, renaud.guillemin@upmc.fr

Wayne C. Stolte
University of Nevada, Las Vegas, wcstolte@lbl.gov

Thomson-resonant interference effects in elastic x-ray scattering near the Cl *K* edge of HCl

S. Carniato,[1,2] P. Selles,[1,2] L. Journel,[1,2] R. Guillemin,[1,2] W. C. Stolte,[3] L. El Khoury,[1,2] T. Marin,[1,2] F. Gel'mukhanov,[4] D. W. Lindle,[3] and M. Simon[1,2]
[1]*UPMC, Université Paris 06, LCPMR, 11 rue Pierre et Marie Curie, 75231 Paris Cedex 05, France*
[2]*CNRS, LCPMR (UMR7614), 11 rue Pierre et Marie Curie, 75231 Paris Cedex 05, France*
[3]*Department of Chemistry, University of Nevada, Las Vegas, Nevada 89154, USA*
[4]*Theoretical Chemistry, Roslagstullsbacken 15, Royal Institute of Technology, S-106 91 Stockholm, Sweden*

(Received 26 July 2012; accepted 19 August 2012; published online 7 September 2012)

We experimentally observed interference effects in elastic x-ray scattering from gas-phase HCl in the vicinity of the Cl *K* edge. Comparison to theory identifies these effects as interference effects between non-resonant elastic Thomson scattering and resonant Raman scattering. The results indicate the non-resonant Thomson and resonant Raman contributions are of comparable strength. The measurements also exhibit strong polarization dependence, allowing an easy identification of the resonant and non-resonant contributions. © *2012 American Institute of Physics*. [http://dx.doi.org/10.1063/1.4749574]

I. INTRODUCTION

Over the past few decades, with the advent of new-generation x-ray sources and detectors, the technique of resonant x-ray scattering (RXS) has developed from fundamental pioneering studies[1–4] into a powerful tool that is now used regularly to study atoms,[5,6] molecules,[7–15] liquids,[16,17] solids,[18,19] buried interfaces, and even complex multi-component systems with practical applications, e.g., solar cells.[20] By itself, the use of x-rays yields the advantage of chemical sensitivity because the primary interactions are with core electrons, which are tightly bound to specific elements in a sample and easily distinguishable by their binding energies. At a fundamental level, the well-known Kramers-Heisenberg formalism[21] allows for a detailed understanding of RXS phenomena such as nonlinear dispersion,[7,13,14] electronic state lifetime interference,[10] polarization of molecular fluorescence,[8,9,15] etc. Within this framework, resonant Raman and non-resonant Thomson contributions must be included explicitly in order to understand and quantitatively analyze elastic x-ray-scattering measurements. They are coherently superimposed so that their interference effects are expected to be ubiquitous in gas-, liquid-, and solid-phase RXS processes.

Such interference effects are largely identified in most RXS experiments in the solid-phase domain. For example, effects due to Thomson scattering have been seen in solid-state x-ray diffraction from CeB_6 near the Ce L_3 absorption edge[22] and attributed to the anisotropic charge distribution in the solid. More generally, in RXS interference techniques these effects are used to reinforce the sensitivity to specific electronic parameters in the material. Thus, they have been applied to study charge and orbital ordering in complex systems (single-layered perovskite or superconductor).[23] Interference effects are also a key phenomenon in multi-wavelength anomalous dispersion (MAD) technique exploiting resonance or anomalous scattering close to an edge.[24,25] They are nearly always present in diffraction anomalous fine structure (DAFS) measuring elastic Bragg reflection intensities versus photon energy.[26]

In gas phase, orientation effects in HCl RXS[27] and interference between Thomson and resonant scattering in CO molecular system[28] have been theoretically predicted, but never observed experimentally. However, recent resonant inelastic soft-x-ray scattering observation of strong Thomson scattering affecting spectral profiles and scattering anisotropy in dioxygen molecule breaks conventional wisdom that Thomson effects are negligible compared to resonant scattering in light elements.[11,12] Following this recent progress, it is highly interesting to study other examples beside the model case of O_2 where such effect is expected to be strong.

In this article, we present the showcase example of elastic x-ray scattering near the Cl *K* edge of gas-phase HCl. We demonstrate that Thomson scattering is not negligible compared to resonant-Raman scattering, and that it is essential to properly interpret scattering cross sections near core-level thresholds. Interference effects between the two processes are depicted schematically in Fig. 1. They are strongly evidenced experimentally as a Fano-like profile in elastic-scattering cross sections in the vicinity of the Cl $1s^{-1} \rightarrow 6\sigma^*$ molecular resonance. Detailed theoretical analysis is provided and confirms these interference effects. In addition, the different resonant channels themselves (i.e., scattering through the molecular resonance and through higher lying $1s^{-1}$–Rydberg states as well as through the $1s^{-1}$ continuum) interfere with one another due to the rather large widths of the Cl $1s^{-1}$ vacancy states.[10]

II. EXPERIMENTAL DETAILS

The experimental data were obtained using the polarized-x-ray-emission endstation at the Advanced Light Source in Berkeley, California, which has been described in detail elsewhere.[9,15,29] One significant modification is that the

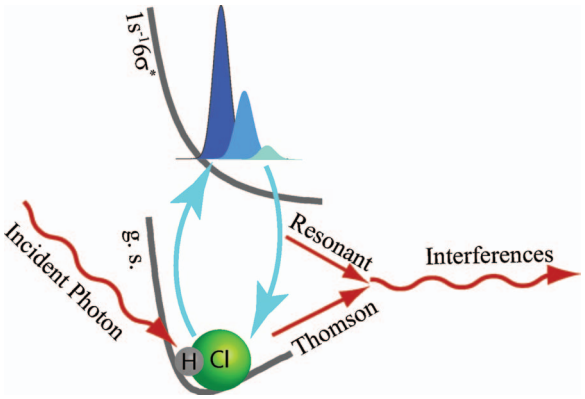

FIG. 1. Schematic illustration of the interference between Thomson scattering and x-ray resonant-Raman scattering from HCl.

gas-sample cell now has a single silicon-nitride window oriented at 50° with respect to the incident x-ray beam that functions as both an entrance and an exit window for the incident and scattered x-rays. This geometry minimizes self-absorption by the sample, a condition required for accurate measurements of elastic scattering. The instrument also is designed to accurately monitor the incoming photon flux and sample pressure. All of these capabilities are necessary for precise measurements of elastic scattering.

Both the beamline monochromator and the x-ray spectrometer use Si(111) crystals to disperse the incident and scattered x-rays, for which the Bragg angle near the Cl *K* edge is 44.5°, close to the x-ray Brewster angle of 45°. Hence, the incident light is highly linearly polarized (more than 99%), and the spectrometer effectively acts as a polarimeter for the scattered x-rays.[15] Two complementary geometries were achieved by rotating the spectrometer with respect to the gas cell and the remainder of the apparatus: (1) the parallel geometry, in which the polarization vectors of the incident and scattered x-rays, $\mathbf{e}_1$ and $\mathbf{e}_2$, lie along the same axis; and (2) the perpendicular geometry, in which $\mathbf{e}_1$ and $\mathbf{e}_2$ are 90° to one another. The RXS spectra are then collected by tuning the x-ray spectrometer to the elastic-scattering energy region and performing measurements as a function of the incident energy for the two geometries. Finally, for this work, the energy width of the incident x-ray beam was 0.50 eV, similar in magnitude to the 0.64 eV lifetime of the HCl $1\,s^{-1} \rightarrow 6\sigma^*$ molecular resonance ($\hbar\omega^* = 2823.5$ eV).

III. COMPUTATIONAL DETAILS

A. Methodology

The final state of the photon-in (ω_1)-photon-out (ω_2) process remains the initial electronic ground state, although the molecule may not be left in its fundamental $\nu = 0$ vibrational level. The rough doubly differential cross section is given by

$$\sigma(\omega_1, \omega_2) = \frac{\omega_2}{\omega_1} r_0^2 \sum_\nu |F_\nu(\omega_1, \omega_2)|^2\, \delta(\omega_1 - \omega_2 - \epsilon_\nu + \epsilon_0), \tag{1}$$

where ϵ_ν refers to the vibrational energy of the final state. Each scattering amplitude F_ν can be written as a coherent contribution of three distinct components: a non-resonant Thomson scattering (T); a resonant D contribution from the dissociative $1\,s^{-1}6\sigma^*$ state; and a resonant R contribution from both the $1\,s^{-1}$ bound Rydberg and continuum states. The latter R contribution can be subdivided into two parts of different molecular symmetry, R^σ and R^π. Explicitly, the scattering amplitudes are

$$F_\nu = (\mathbf{e}_2 \cdot \mathbf{e}_1)\rho(\mathbf{q})\delta_{\nu,0} + \varpi_z\, \mathcal{D}_\nu + [\varpi_z\, \mathcal{R}_\nu^\sigma + (\mathbf{e}_2 \cdot \mathbf{e}_1 - \varpi_z)\mathcal{R}_\nu^\pi]. \tag{2}$$

The Thomson form factor $\rho(\mathbf{q})$ is the Fourier transform of the electron density in the initial state, $\mathbf{q} = \mathbf{k}_2 - \mathbf{k}_1$ being the scattering vector.

The kinematic factor $\varpi_z = (\mathbf{e}_2 \cdot \hat{R})(\mathbf{e}_1 \cdot \hat{R})$ depends on the molecular orientation, $\hat{R}$ being the unit vector along the molecular axis.

To simplify the notations, the (ω_1, ω_2) dependence has been omitted in the amplitudes.

For a fixed-in-space HCl molecule, the form factor can be expanded on Legendre polynomials

$$\rho(\mathbf{q}) = \sum_l \rho_\ell(q) P_\ell(\hat{\mathbf{q}} \cdot \hat{\mathbf{R}}). \tag{3}$$

Each radial factor $\rho_\ell(q)$ is then given by

$$\rho_\ell(q) = \frac{2\ell + 1}{2} \sum_{im} N_{im} \int d\hat{\mathbf{q}} \langle \psi_{im} | e^{\imath \mathbf{q}\cdot\mathbf{r}} | \psi_{im} \rangle P_\ell(\hat{\mathbf{q}} \cdot \hat{\mathbf{R}}), \tag{4}$$

where N_{im} is the number of electrons in the ψ_{im} molecular orbital implied in the fundamental electronic state.

The resonant contributions are expressed according to the Kramers-Heisenberg formula, within the dipolar approximation

$$\mathcal{R}_\nu^{\sigma,\pi} = \sum_{nj} (\omega_n + \epsilon_{nj} - \epsilon_0)(\omega_n + \epsilon_{nj} - \epsilon_\nu) \langle \nu | \mathrm{d}_n^* | j \rangle \langle j | \mathrm{d}_n | 0 \rangle \times \left[\frac{1}{\omega_1 - \omega_n - \epsilon_{nj} + \epsilon_0 - \imath\Gamma_n} + \frac{1}{\omega_2 + \omega_n + \epsilon_{nj} - \epsilon_0} \right]. \tag{5}$$

Here, Γ_n is the nth $1\,s^{-1}$ core hole state lifetime and $\omega_n + \epsilon_{nj}$ the energy of its jth vibrational level. The sum is performed over the $1\,s^{-1}ns\sigma^1$ and $1\,s^{-1}np\sigma^1$ Rydberg states for the σ symmetry (over the $1\,s^{-1}np\pi^1$ ones for the π symmetry) and their vibrational j levels. The $1\,s^{-1}n\ell$ Rydberg states for $n \geq 5$ are modelized together with the continuum, which is discretized. Each $\mathcal{D}_\nu$ amplitude is given by the same equation after the following replacements $\sum_{nj} \rightarrow \int d\epsilon$, $|j\rangle \rightarrow |\epsilon\rangle$, $\mathrm{d}_n \rightarrow \mathrm{d}_{\sigma^*}$, $\omega_n + \epsilon_j \rightarrow \omega^* + \epsilon$.

Experimental observables are then built from the rough doubly differential cross sections written in Eq. (1). First of all, an averaging over all molecular orientations is performed. The average cross sections obtained for perpendicular and parallel geometries are, respectively,

$$\overline{\sigma}_\perp(\omega_1, \omega_2) = \frac{r_0^2}{15} \sum_{\nu=0}^{\infty} \frac{\omega_2}{\omega_1} \left| \mathcal{D}_\nu + \mathcal{R}_\nu^\sigma - \mathcal{R}_\nu^\pi \right|^2 \delta(\omega_1 - \omega_2 - \epsilon_\nu + \epsilon_0)\,, \tag{6}$$

$$\overline{\sigma}_{\parallel}(\omega_1,\omega_2) = \frac{r_0^2}{15}\sum_{\nu=0}\frac{\omega_2}{\omega_1}\{\mathcal{O}_T\,\delta_{\nu 0} + \mathcal{O}_{DD} + \mathcal{O}_{RR} + \mathcal{O}_{DR}\}\delta(\omega_1-\omega_2-\epsilon_\nu+\epsilon_0). \quad (7)$$

In the perpendicular configuration, all the Thomson contributions are made inoperative by the molecular orientation averaging. The cross section is built on the coherent superposition of only two resonant-Raman contributions

$$\overline{\sigma}_{\perp}(\omega_1,\omega_2) = \frac{r_0^2}{15}\sum_{\nu=0}^{\infty}\frac{\omega_2}{\omega_1}\,|\mathcal{D}_\nu + \Delta\mathcal{R}_\nu|^2\,\delta(\omega_1-\omega_2-\epsilon_\nu+\epsilon_0)\,. \quad (8)$$

More precisely it does not depend on each $\mathcal{R}_\nu^\sigma$ and $\mathcal{R}_\nu^\pi$ amplitude separately, but only on their difference $\Delta\mathcal{R}_\nu = \mathcal{R}_\nu^\sigma - \mathcal{R}_\nu^\pi$.

In the parallel configuration, the Thomson contributions appear in the $\mathcal{O}_T$ factor that contains direct Thomson-Thomson *T-T* (first term, first line of Eq. (9)) as well as Thomson-resonant interference terms, namely *T-D* (second term, first line of Eq. (9)), and *T-R* terms (second line of Eq. (9))

$$\mathcal{O}_T = 15\sum_\ell \frac{|\rho_\ell|^2}{2\ell+1} + 2\mathrm{Re}[(5\rho_0-\rho_2)\mathcal{D}_0^*] + 2\mathrm{Re}[(5\rho_0-\rho_2)\mathcal{R}_0^{\sigma^*} + (10\rho_0+\rho_2)\mathcal{R}_0^{\pi^*}]. \quad (9)$$

The others $\mathcal{O}$ factors are resonant-resonant factors, respectively, *D-D*, *R-R*, and *D-R* factors

$$\mathcal{O}_{DD} = 3|\mathcal{D}_\nu|^2, \quad (10)$$

$$\mathcal{O}_{RR} = 3|\mathcal{R}_\nu^\sigma|^2 + 8|\mathcal{R}_\nu^\pi|^2 + 4\mathrm{Re}(\mathcal{R}_\nu^{\pi*}\mathcal{R}_\nu^\sigma), \quad (11)$$

$$\mathcal{O}_{DR} = 2\,\mathrm{Re}(3\mathcal{R}_\nu^{\sigma*}\mathcal{D}_\nu + 2\mathcal{R}_\nu^{\pi*}\mathcal{D}_\nu). \quad (12)$$

The spectral shape of the incident photon beam is then taken into account as a normalized gaussian with a FWHM of 0.5 eV. Finally, the singly differential cross sections $\sigma(\omega)$ are obtained by integrating over all emission events for a given nominal excitation energy ω. They can be written, respectively, in the perpendicular and parallel geometries as

$$\sigma_\perp(\omega) = \frac{r_0^2}{15}\sum_{\nu=0}^{\infty}\langle|\mathcal{D}_\nu + \mathcal{R}_\nu^\sigma - \mathcal{R}_\nu^\pi|^2\rangle, \quad (13)$$

$$\sigma_\parallel(\omega) = \frac{r_0^2}{15}\sum_{\nu=0}^{\infty}\langle\mathcal{O}_T\rangle\,\delta_{\nu 0} + \langle\mathcal{O}_{DD}\rangle + \langle\mathcal{O}_{RR}\rangle + \langle\mathcal{O}_{DR}\rangle. \quad (14)$$

The bracket notation indicates the convolution with the incident beam profile, the integration over all emission events making the singly differential cross section independent of the spectrometer resolution. For example,

$$\langle\mathcal{O}_{DD}\rangle = \int d\omega_1 \frac{\omega_1-\epsilon_\nu+\epsilon_0}{\omega_1} \times\Phi(\omega_1-\omega)\mathcal{O}_{DD}(\omega_1,\omega_1-\epsilon_\nu+\epsilon_0). \quad (15)$$

B. Molecular parameters

The potential curve for the ground state has been approximated by a Morse potential the parameters of which have been published previously.[8,9] Potential curves for $1s^{-1}$ core excited states and electronic wavefunctions (including that of the ground state) were computed using post Hartree-Fock configuration interaction (CISD). A large augmented correlation-consistent-core-valence polarized quadruple zeta atomic Cartesian-Gaussian basis set (aug-cc-pCVQZ)[10] limited to *s*, *p*, and *d* waves centered on Cl and H atoms was used. To account for relaxation of the valence orbitals, a set of Hartree-Fock–self-consistent field (HF-SCF) orthogonal orbitals optimized for the Cl $2s^{-1}\sigma^*$ intermediate core-excited state was included in the CI active space.[10]

For all core-excited potentials, vibrational wave functions were calculated using a one dimensional hamiltonian model as described previously.[10] Even if the dipolar approximation is demonstrated to not be strictly justified (see later in the text comments on the calculations of the Thomson form factors), the transition momenta to core excited states were computed within this approximation. The values recorded in the length gauge allowed to recover with an excellent agreement the experimental absorption spectrum as displayed in Figure 2(b).

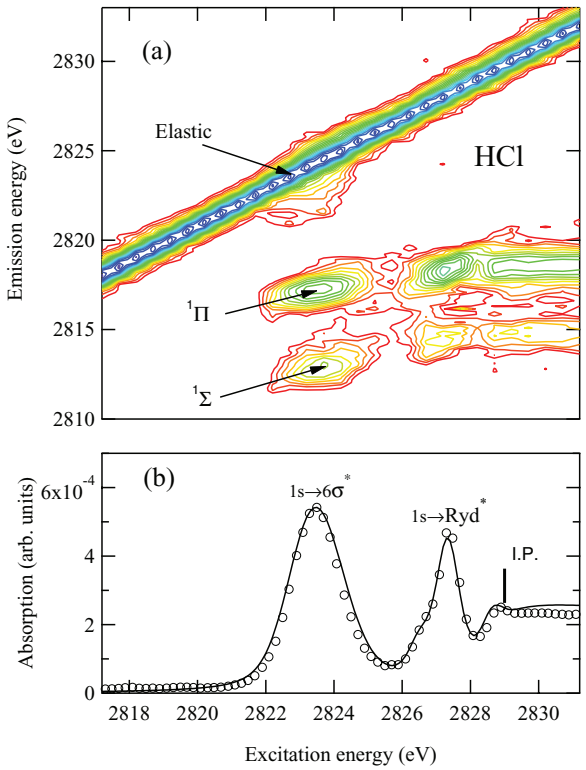

FIG. 2. (a) 2D map of the KV emission in HCl as a function of excitation energy around the $1s^{-1} \rightarrow 6\sigma^*$ molecular resonance ($\hbar\omega^* = 2823.5$ eV) up to Cl 1*s* ionization threshold ($\hbar\omega = 2829$ eV). Data were recorded in the parallel geometry. The elastic x-ray scattering appears as a continuous profile dispersing linearly with the incoming photon energy. (b) Absorption cross sections in arbitrary units as a function of incoming photon energy in eV. Data points are shown as circles, and theoretical results as a solid line. They are normalized at the maximum of the signal.

From the $1s^{-1}5s$ Rydberg state up to the continuum, all the potential curves were assumed parallel. Their minimum corresponds nearly to the ground state equilibrium distance. The density of states and the transition momenta were numerically adjusted to match the relative intensity measured above the Cl *K*-edge in the photoabsorption spectra. The agreement between theoretical and experimental absorption cross sections is excellent, as displayed in Fig. 2(b).

The $\rho_\ell(q)$ radial factors were calculated thanks to Gauss-Legendre and Gauss-Laguerre quadratures. They were found to vary by about 0.5% in the energy range of interest, and were thus held constant in the calculations. At the resonance energy ω^*, the six first moduli were obtained to be: $\rho_0 = 13$, 51, $\rho_1 = -0.156\,i$, $\rho_2 = -0.358$, $\rho_3 = -0.404\,i$, $\rho_4 = 0.174$ and $\rho_5 = 0.029\,i$. The ρ_0 value is not equal to the number of electrons in the HCl molecule $Z = 18$, indicating that the dipolar approximation is not strictly justified.

IV. RESULTS AND DISCUSSION

K V emission from HCl was recorded by varying the excitation photon energy between 2817.5 and 2832 eV in the energy region containing the $1s \rightarrow 6\sigma^*$ resonance and the Cl $1s$ ionization threshold. Figure 2 shows the 2D map of the *KL* spectra recorded as a function of excitation energy. Three "lines" are visible in the 2D map corresponding to the $^1\Sigma$ state, the $^1\Pi$ state, and the elastic emission.[7] The elastic scattering appears as a continuous profile dispersing linearly with the incoming photon energy. The singly differential cross sections were obtained by integrating all the events in the elastic profile along a vertical line corresponding to a given excitation energy. Figures 3 and 4 display a comparison between experimental and theoretical singly differential cross sections obtained in the parallel and perpendicular geometries, respectively. An absolute scale given in atomic units is now provided by the theoretical calculations. In the parallel geometry,

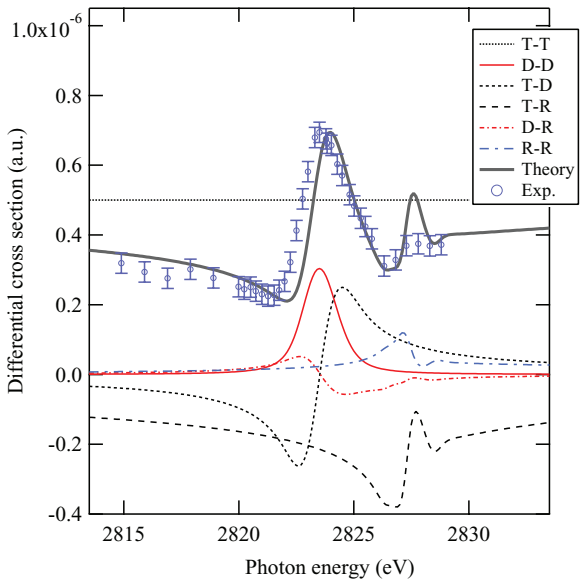

FIG. 3. Singly differential cross sections in atomic units as a function of incoming photon energy in the parallel geometry.

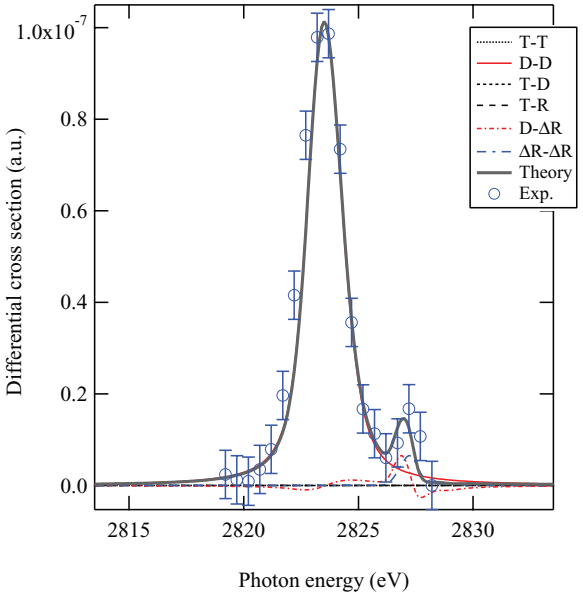

FIG. 4. Singly differential cross sections in atomic units as a function of incoming photon energy in the perpendicular geometry.

a background of an amount of 40% was subtracted from the rough experimental intensities before they were normalized to the theoretical cross sections at the maximum of the signal. The origin of this background may probably be partly due to elastic scattering by the window of the gas cell as already suggested.[11] We also found that contribution from the $1s^{-1}$ continuum left a sensitive imprint on the low energy side. So that modifying the modelization of this continuum induced a different ratio between the mean maximum and the left tail and consequently a different normalization procedure for the experimental data. In the most favourable case, a background of only 25% had to be subtracted from the measured intensities. In the perpendicular geometry, the experimental results were normalized to the theoretical ones to the maximum of the signal. Both data sets exhibit a dominant peak near the Cl $1s^{-1} \rightarrow 6\sigma^*$ resonance. A secondary peak in the vicinity of 2827 eV is also observable in both theoretical and experimental perpendicular cross sections and in theoretical parallel cross sections. It is however hardly distinguishable in experimental parallel cross sections. This peak corresponds to the excitation of Rydberg $1s^{-1}4n$ states. At the same time, significant differences are clearly identifiable between the two geometries. The most important singular characteristic concerns the asymmetric Fano-like profile, which is unambiguously enlightened in the parallel geometry on both theoretical and experimental cross sections. It displays a local minimum at 2821 eV and a shoulder at 2825 eV. This profile is the signature of interferences between Thomson and resonant scatterings. These interference effects are also responsible for the shift towards the high energy side of the main maximum in the parallel geometry compared to the perpendicular geometry. In this latter case, the peak appears at the resonance energy $\omega^* = 2823.5$ eV, because it is free of Thomson contributions and is quite exclusively made by the *D-D* contribution, as shown in Fig. 4. In the parallel geometry, theoretical cross sections clearly highlight a 0.4 eV offset.

Experimental cross sections show a slightler shift (around 0.1 eV). Discrepancy about this shift may be due once again to the modelization of the continuum the effects of which are enhanced by its interference with the non resonant Thomson contribution.

The whole set of properties of the singly differential cross sections can be well understood thanks to the details provided by the calculated different contributions displayed in Figs 3 and 4. Looking first at the parallel geometry (Fig. 3), one finds the remarkable result that the largest contributions are due to Thomson scattering, both through the direct (*T*-*T*) term and the Thomson-resonant interference terms (*T*-*D* and *T*-*R*). This unusual behavior has two physical origins: first, the resonant contribution is somewhat lessened by the large Franck-Condon width ($\approx$1.6 eV) of the Cl $1s^{-1}6\sigma^*$ dissociative state, then the Thomson scattering is relatively strong because almost all 18 electrons in the molecule contribute. In this parallel geometry, the interference terms appear clearly to be responsible for the Fano-like profile of the main peak, adding destructively on the low-energy side and constructively on the high-energy side.

In the perpendicular geometry (Fig. 2), Thomson scattering is inoperative. The largest component comes from the direct *D*-*D* scattering by the molecular resonance; its contribution is responsible by itself for the main peak. As already explained, this property is responsible for the location of the maximum at the resonance energy. The magnitude and shape of the secondary peak at 2827 eV originate from the (*D*-ΔR) and (ΔR-ΔR) contributions and are thus tied to the anisotropy of the Rydberg and continuum states. This secondary peak would be absent if $\Delta\mathcal{R}_v$ were zero.

All these properties are confirmed by the overall excellent agreement between experiment and theory in both geometries.[11] One questionable point remains to be discussed; it concerns the secondary maximum in the parallel geometry around 2827 eV. More experimental points in this region would be necessary to check definitively the height of this local maximun. If the secondary maximum there was confirmed to be very low while the experimental absorption spectrum displayed in Fig. 2(b) exhibits around 2827 eV an important maximum due to $4s$ and $4p$ contributions, we should consider a theoretical description extended beyond the dipolar approximation, as suggested by the values obtained for the Thomson factors. In such a non dipolar description, the Rydberg $n=4$ contributions could interfere destructively with each other or/and with the Thomson contribution while they add incoherently in the building of the absorption cross sections.

In conclusion, elastic x-ray scattering was investigated around the Cl *K* edge of HCl. The scattering cross sections and profiles exhibit significant polarization sensitivity, measured experimentally by selecting parallel or perpendicular geometries for the polarization of the incident and scattered x-rays. The two geometries are complementary as they are able thanks to a detailed comparison between experiment and theory to enlighten different pertinent properties of the elastic scattering. In the parallel geometry strong interference effects between classical non-resonant Thomson scattering and resonant scattering through both the $6\sigma^*$ state, the Rydberg core-excited states, and the $1s^{-1}$ continuum, were identified. Their strength was shown to be due to a comparable magnitude of the Thomson and resonant-scattering contributions. Interference effects between Thomson and resonant scatterings are certainly a general phenomenon in the x-ray regime. They can be used as a stringent test for theoretical models. Definitively, Thomson scattering will need to be considered in interpreting elastic scattering from any sample, including gases, liquids, and condensed phases. On the other hand, Thomson scattering may be a drawback as it strongly affects the vibrational progression of the elastic peak, preventing to quantify the ultra fast nuclear motion.[7,30] Then the perpendicular geometry which is free of Thomson contributions becomes perfectly suited for such a study. Interference between resonant contributions trough different Rydberg and/or continuum states are also accessible via detailed comparison of theory and experiment. More particularly, anisotropy of Rydberg and continuum states was evidenced in the perpendicular geometry.

[1] D. W. Lindle, P. L. Cowan, R. E. LaVilla, T. Jach, and R. D. Deslattes, Phys. Rev. Lett. **60**, 1010 (1988).
[2] R. Mayer, D. W. Lindle, S. H. Southworth, and P. L. Cowan, Phys. Rev. A **43**, 235 (1991).
[3] S. H. Southworth, D. W. Lindle, R. Mayer, and P. L. Cowan, Phys. Rev. Lett. **67**, 1098 (1991).
[4] D. W. Lindle, P. L. Cowan, T. Jach, R. E. LaVilla, and R. D. Deslattes, Phys. Rev. A **43**, 2353 (1991).
[5] P. A. Raboud, M. Berset, J.-Cl Dousse, Y.-P Maillard, O. Mauron, J. Hoszowska, M. Polasik, and J. Rzadkiewicz, Phys. Rev. A **65**, 062503 (2002).
[6] M. Žitnik, M. Kavčič, K. Bučar, A. Mihelič, M. Štuhec, J. Kokalj, and J. Szlachetko, Phys. Rev. A **76**, 032506 (2007).
[7] M. Simon, L. Journel, R. Guillemin, W. C. Stolte, I. Minkov, F. Gel'mukhanov, P. Sałek, H. Ågren, S. Carniato, R. Taïeb, A. C. Hudson, and D. W. Lindle, Phys. Rev. A **73**, 020706(R) (2006).
[8] R. Guillemin, S. Carniato, W. C. Stolte, L. Journel, R. Taïeb, D. W. Lindle, and M. Simon, Phys. Rev. Lett. **101**, 133003 (2008).
[9] S. Carniato, R. Guillemin, W. C. Stolte, L. Journel, R. Taïeb, D. W. Lindle, and M. Simon, Phys. Rev. A **80**, 032513 (2009).
[10] M. Kavčič, M. Žitnik, K. Bučar, A. Mihelič, S. Carniato, L. Journel, R. Guillemin, and M. Simon, Phys. Rev. Lett. **105**, 113004 (2010); D. E. Woon and T. H. Dunning, Jr., J. Chem. Phys. **98**, 1358 (1993).
[11] F. Hennies, A. Pietzsch, M. Berglund, A. Föhlisch, T. Schmitt, V. Strocov, H. O. Karlsson, J. Andersson, and J.-E. Rubensson, Phys. Rev. Lett. **104**, 193002 (2010).
[12] A. Pietzsch, Y.-P. Sun, F. Hennies, Z. Rinkevicius, H. O. Karlsson, T. Schmitt, V. N. Strocov, J. Andersson, B. Kennedy, J. Schlappa, A. Föhlisch, J.-E. Rubensson, and F. Gel'mukhanov, Phys. Rev. Lett. **106**, 153004 (2011).
[13] T. Marchenko, L. Journel, T. Marin, R. Guillemin, S. Carniato, M. Žitnik, M. Kavčič, K. Bučar, A. Mihelič, W. Cao, and M. Simon, J. Chem. Phys. **134**, 144308 (2011).
[14] L. El Khoury, L. Journel, R. Guillemin, S. Carniato, W. C. Stolte, T. Marin, D. W. Lindle, and M. Simon, J. Chem. Phys. **136**, 024319 (2012).
[15] R. Guillemin, W. C. Stolte, L. Journel, S. Carniato, M. N. Piancastelli, D. W. Lindle, and M. Simon, Phys. Rev. A. **86**, 013407, (2012).
[16] M. Odelius, H. Ogasawaram D. Nordlund, O. Fuchs, L. Weinhardt, F. Maier, E. Umbach, C. Heske, Y. Zubavichus, M. Grunze, J. D. Denlinger, L. G. M. Pettersson, and A. Nilsson, Phys. Rev. Lett **94**, 227401 (2005).
[17] O. Fuchs, M. Zharnikov, L. Weinhardt, M. Blum, M. Weigand, Y. Zubavichus, M. Bär, F. Maier, J. D. Denlinger, C. Heske, M. Grunze, and E. Umbach, Phys. Rev. Lett. **100**, 027801 (2008).
[18] J. Guo, Int. J. Nanotechnol. **1–2**, 193 (2004).
[19] J.-P. Rueff and A. Shukla, Rev. Mod. Phys. **82**, 847 (2010).
[20] C. Heske, D. Eich, R. Fink, E. Umbach, T. van Buuren, C. Bostedt, L. J. Terminello, S. Kakar, M. M. Grush, T. A. Callcott, F. J. Himpsel, D. L.

Ederer, R. C. C. Perera, W. Riedl, and F. Karg, Appl. Phys. Lett. **74**, 1451 (1999).
[21]H. A. Kramers and W. Heisenberg, Z. Phys. **31**, 681 (1925).
[22]T. Nagao and J. Igarashi, J. Phys. Soc. Jpn. **72**, 2381 (2003).
[23]Y. Murakami, H. Kawada, H. Kawata, M. Tanaka, T. Arima, Y. Moritomo, and Y. Tokura, Phys. Rev. Lett. **80**, 1932 (1998).
[24]W. A. Hendrickson, Science **254**, 51 (1991).
[25]W. A. Hendrickson and C. M. Ogata, Methods Enzymol. **276**, 494 (1997).
[26]H. Stragier, J. O. Cross, J. J. Rehr, L. Sorensen, C. E. Bouldin, and J. C. Woicik, Phys. Rev. Lett. **69**, 3064 (1992).
[27]V. A. Yavna, A. N. Hopersky, A. M. Nadolinsky, and S. A. Yavna, J. Phys. B **33**, 3249 (2000).
[28]F. Gel'mukhanov and H. Ågren, Phys. Rev. A **56**, 2676 (1997).
[29]A. C. Hudson, W. C. Stolte, D. W. Lindle, and R. Guillemin, Rev. Sci. Instrum. **78**, 053101 (2007).
[30]F. Gel'mukhanov, P. Sałek, T. Privalov, and H. Ågren, Phys. Rev. A **59**, 380 (1999).